4.6 Supplementary tables

Anatomical:					
Parameter	Lit. Val.	Fit type	NAOMi Val.	Unit	Refs
Neural density	9.20E+04	Direct	–	mm^{-3}	[58]
Axonal diameter	0.3	Direct	–	μm	[58]
Fraction vasculature	0.01-0.04	Indirect	0.032	–	[58, 75, 76]
Fraction cell bodies	0.12	Indirect	0.135	–	[58]
Fraction neuropil	0.84	Indirect	0.833	–	[58]
Fraction dendrites*	0.294	Indirect	0.223	–	[58]
Fraction other (fluorescing)*	0.401	Indirect	0.33	–	[58]
Fraction other (not fluorescing)*	0.293	Indirect	0.28	–	[58, 77]
Vessel radius (capillary)	2.00E+00	Direct	–	μm	[56]
Vessel radius (penetrating)	10 (9,11)	Direct	–	μm	[56]
Vessel radius (surface)	4-30	Direct	–	μm	[56]
Vessel length	50	Indirect	50	μm	[56]
Vessel orientation	Uniform	Indirect	Uniform	–	[56]
Vascular density	1-3	Indirect	2	%	[56, 58, 75, 76]
Penetrating vessel density	30†	Direct	–	mm^{-2}	[56]
Somatic volume*	1.80E+03†	Indirect	1.80E+03	μm^3	[78]
Nuclear volume*	800†	Indirect	800	μm^3	[78]
Cytoplasm volume*	1000†	Indirect	1000	μm^3	[78]
Somatic radius*	6.25-7.5†	Indirect	7.5	μm	[60, 78]
Nuclear radius*	6†	Indirect	6	μm	[78]
Fraction cell bodies	0.12	Indirect	0.135	–	[58]
Basal dendrite endings	23-25†	Direct	–	–	[59–61]
Basal dendrite diameter	0.7	Direct	–	μm	[79]
Basal dendrite length	100-160†	Indirect	105	μm	[59–61]
Apical dendrite endings	6-20†	Direct	–	–	[59, 60]
Apical dendrite diameter	1-2	Direct	–	μm	[80]
Rall exponent	1.5	Direct	–	–	[116]
*Adjusted for shrinkage: 31% [87],†Value estimated from data in the literature					

Supplementary Table 1: Anatomical parameters used for *in-silico* simulation of neural activity in layer II/III of mouse primary visual area V1. Values for each parameter were either directly found in the literature or estimated from published data (entries with a †). The third column indicates whether these parameters were set directly in NAOMi, or were fit indirectly by setting other simulation parameters. In the latter cases, the measured values from a simulated NAOMi volume are shown for comparison, indicating that the simulated anatomy matches measured anatomical statistics.

Fluorescence model:					
Parameter	Anat. Val.	Fit type	NAOMi Val.	Unit	Refs
GCaMP6f binding affinity K_d	290	Direct	–	nMol	[70]
Baseline Ca^{2+} concentration	50.00	Direct	–	nMol	[68]
Ca^{2+} axon diffusion constant γ	2800	Direct	–	s^{-1}	[67, 81, 84]
Endogenouse Ca^{2+} binding ratio k_s	100,110	Direct	110	AU	[67, 81–83]
Ca^{2+} diffusion constant γ	1800	Data fit	292.3	s^{-1}	[67, 81, 82]
Onset time constant τ_{on}	–	Data fit	98.62	AU	–
Decay time constant τ_{off}	–	Data fit	0.85	AU	–
GCaMP6f Hill eqn. exponent n_h	2.7	Direct	–	AU	[70]
GCaMP6f Hill eqn. amplitude	25.2	Direct	–	F	[70]
Indicator concentration	10-200	Direct	10	μM	[68, 85, 86]

Supplementary Table 2: Fluorescence parameters used for *in-silico* simulation of neural activity in layer II/III of mouse primary visual area V1. Values for each parameter were either directly found in the literature or estimated from published data (entries with a †). The third column indicates whether these parameters were set directly, or were fit indirectly by setting other simulation parameters. In the latter cases, the measured values simulated fluorescence traces are shown for comparison, indicating a good match between the NAOMi simulation and known activity statistics.

4.7 Supplementary figures

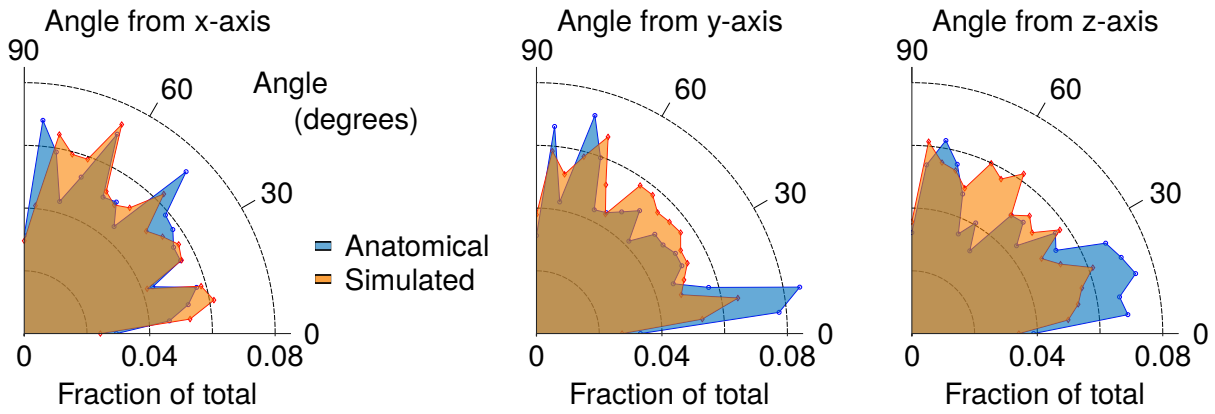

Supplementary Figure 1: Histograms comparing the distribution of simulated vasculature orientation (angles from the x- y- and z-axes) to distributions observed in data from [106].

Optical:			
Parameter	Value	Unit	Refs
Refractive index (tissue average)	1.35	–	[117]
Refractive index (SD)	0.02	–	[78, 117]
Scatter size	[0.51 1.56 4.52 14.78]	μm	[78, 102], See Methods
Scatter weight	[0.57 0.29 0.19 0.15]	–	[78, 102], See Methods
Wavelength λ	920	nm	[118]
System aberrations (astigmatism)	0.1	λ	See Methods
System aberrations (spherical)	0.12	λ	See Methods
Hemoglobin absorption	0.00674*log(10)	–	[108], See Methods
Objective NA	0.8	–	[119]
PMT QE	0.4	–	[120]
eGFP Quantum Yield	0.6	–	[118]
Δ, baseline F_0	2	GM	[118]
Δ, saturation F_{max}	35	GM	[118]
Sech pulse shape	0.588	–	[121]
Ti:S rep rate	80	MHz	[121]
Ti:S pulse width	140	fs	[121]

Supplementary Table 3: Optical parameters used for *in-silico* simulation of two-photon microscopy scanning.

Scanning:			
Parameter	Value	Unit	Refs
PMT dynode model			[122], See Methods
PMT Poisson-Gauss	1, 100 (mean photon,electronic) 0.23, 2300 (std photon,electronic)	counts	See Methods
Bleed-through probability	0.3	–	See Methods
Bleed-through weight	0.4	V*s	See Methods
PMT darkcount mean	0.05	counts	See Methods

Supplementary Table 4: Scanning parameters used for *in-silico* simulation of two-photon microscopy scanning.

Other parameters:					
Parameter	Anat. Val.	Fit type	NAOMi Val.	Unit	Refs
Axonal diameter	0.3	Direct	–	μm	[58]
Fraction vasculature	0.01-0.04	Indirect	0.032	–	[58, 75, 76]
Fraction cell bodies	0.12	Indirect	0.135	–	[58]
Fraction neuropil	0.84	Indirect	0.833	–	[58]
Fraction spines*	0.118	Indirect	0	–	[58]
Fraction dendrites*	0.294	Indirect	0.223	–	[58]
Fraction Axons*	0.283	Indirect	0.33	–	[58]
Fraction Glia*	0.0924	Indirect	0.08	–	[58]
Fraction extracellular	0.2	Direct	0.2	–	[77]
*scaled to full volume [87]					

Supplementary Table 5: Detailed fractional volume of components

40 mW power	CNMF (1091 total)			Suite2p (661 total)			PCA/ICA (265 total)		
Corr. cutoff	>0.1	>0.3	>0.5	>0.1	>0.3	>0.5	>0.1	>0.3	>0.5
Paired	704	522	338	519	479	423	170	152	144
Unique	566	438	303	366	335	292	152	139	137
Doubled	95	54	27	68	64	58	11	9	7

Supplementary Table 6: Results of automated calcium imaging video segmentation as applied to simulated data generated from NAOMi. Of the total number of components isolated, only a fraction ($\approx 30\% - 50\%$) unique, true cells in the scanned volume strongly matched the found components.

40 mW power	Unique Cells found		
Corr. cutoff	>0.1	>0.3	>0.5
CNMF (1091 total)	566	438	303
Suite2p (1091 total)	366	335	292
PCA/ICA (265 total)	152	139	137
CNMF Only	238	69	28
Suite2p Only	43	26	17
PCA/ICA Only	13	2	3
CNMF & Suite2p	321	307	273
CNMF & PCA/ICA	144	136	134
Suite2p & PCA/ICA	134	137	134
All algorithms	137	135	132

Supplementary Table 7: Results of automated calcium imaging video segmentation as applied to simulated data generated from NAOMi. While sets of found components largely overlapped between algorithms, each method's design allowed for the extraction of slightly different cell activities.

40 mW power	Unique Cells found		
Corr. cutoff	>0.1	>0.3	>0.5
Ideal (8117 total)	2088	817	415
Ideal & not CNMF	1523	383	120
Ideal & not Suite2p	1722	483	128
Ideal & not PCA/ICA	1936	678	278
CNMF & not Ideal	1	4	8
Suite2p & not Ideal	0	1	5
PCA/ICA & not Ideal	0	0	0

Supplementary Table 8: Results of automated calcium imaging video segmentation as applied to simulated data generated from NAOMi. De-mixing the data using oracle spatial profile knowledge allowed for isolating many more components, indicating that automated methods have room for improvement. Interestingly some algorithms, due to built in denoising not included in the ideal de-mixing, were able to isolate some cell time-traces more accurately.

80 mW power	CNMF (999 total)			Suite2p (639 total)			PCA/ICA (635 total)		
Corr. cutoff	>0.1	>0.3	>0.5	>0.1	>0.3	>0.5	>0.1	>0.3	>0.5
Paired	651	546	460	532	479	462	420	322	292
Unique	579	493	424	413	369	358	337	280	264
Doubled	60	41	30	61	54	53	47	28	20

Supplementary Table 9: Results of automated calcium imaging video segmentation as applied to simulated data generated from NAOMi with 80 mW laser power.

80 mW power	Unique Cells found		
Corr. cutoff	>0.1	>0.3	>0.5
CNMF (999 total)	579	493	424
Suite2p (639 total)	413	369	358
PCA/ICA (635 total)	337	280	264
CNMF Only	198	118	85
Suite2p Only	46	24	22
PCA/ICA Only	90	38	24
CNMF & Suite2p	357	334	325
CNMF & PCA/ICA	261	247	243
Suite2p & PCA/ICA	240	242	240
All algorithms	237	231	229

Supplementary Table 10: Results of automated calcium imaging video segmentation as applied to simulated data generated from NAOMi with 80 mW laser power.

80 mW power	Unique Cells found		
Corr. cutoff	>0.1	>0.3	>0.5
Ideal (8117 total)	3206	1528	904
Ideal & not CNMF	2629	1036	481
Ideal & not Suite2p	2793	1159	546
Ideal & not PCA/ICA	2870	1248	640
CNMF & not Ideal	3	1	1
Suite2p & not Ideal	1	0	0
PCA/ICA & not Ideal	2	0	0

Supplementary Table 11: Results of automated calcium imaging video segmentation as applied to simulated data generated from NAOMi with 80 mW laser power.

40 mW power	CNMF (1091 total)			Suite2p (661 total)			PCA/ICA (265 total)		
Corr. cutoff	>0.1	>0.3	>0.5	>0.1	>0.3	>0.5	>0.1	>0.3	>0.5
Paired	261	212	156	246	230	204	93	84	77
Unique	234	202	151	175	166	143	83	78	76
Doubled	25	10	5	34	28	25	5	3	1

Supplementary Table 12: Somatic component recovery via automated calcium imaging video segmentation as applied to simulated data generated from NAOMi. Of the total number of components isolated, only a fraction ($\approx 30\% - 50\%$) unique, true cells in the scanned volume strongly matched the found components.

40 mW power	Unique Cells found		
Corr. cutoff	>0.1	>0.3	>0.5
CNMF (1091 total)	234	202	151
Suite2p (1091 total)	175	166	143
PCA/ICA (265 total)	83	78	76
CNMF Only	65	44	12
Suite2p Only	8	8	4
PCA/ICA Only	2	0	0
CNMF & Suite2p	167	158	139
CNMF & PCA/ICA	83	78	76
Suite2p & PCA/ICA	81	78	76
All algorithms	81	78	76

Supplementary Table 13: Somatic component recovery via automated calcium imaging video segmentation as applied to simulated data generated from NAOMi. While sets of found components largely overlapped between algorithms, each method's design allowed for the extraction of slightly different cell activities.

40 mW power	Unique Cells found		
Corr. cutoff	>0.1	>0.3	>0.5
Ideal (451 total)	395	248	161
Ideal & not CNMF	161	48	14
Ideal & not Suite2p	220	83	20
Ideal & not PCA/ICA	312	170	85
CNMF & not Ideal	0	2	4
Suite2p & not Ideal	0	1	2
PCA/ICA & not Ideal	0	0	0

Supplementary Table 14: Somatic component recovery via automated calcium imaging video segmentation as applied to simulated data generated from NAOMi. De-mixing the data using oracle spatial profile knowledge allowed for isolating many more components, indicating that automated methods have room for improvement. Interestingly some algorithms, due to built in denoising not included in the ideal de-mixing, were able to isolate some cell time-traces more accurately.

80 mW power	CNMF (999 total)			Suite2p (639 total)			PCA/ICA (635 total)		
Corr. cutoff	>0.1	>0.3	>0.5	>0.1	>0.3	>0.5	>0.1	>0.3	>0.5
Paired	255	226	209	255	238	228	167	146	136
Unique	239	222	206	201	192	186	139	131	128
Doubled	15	4	3	32	24	22	10	7	2

Supplementary Table 15: Somatic component recovery via automated calcium imaging video segmentation as applied to simulated data generated from NAOMi with 80 mW laser power.

80 mW power	Unique Cells found		
Corr. cutoff	>0.1	>0.3	>0.5
CNMF (999 total)	239	222	206
Suite2p (639 total)	201	192	186
PCA/ICA (635 total)	139	131	128
CNMF Only	51	42	33
Suite2p Only	15	11	11
PCA/ICA Only	9	3	2
CNMF & Suite2p	183	178	172
CNMF & PCA/ICA	132	127	124
Suite2p & PCA/ICA	132	128	126
All algorithms	127	125	123

Supplementary Table 16: Somatic component recovery via automated calcium imaging video segmentation as applied to simulated data generated from NAOMi with 80 mW laser power.

80 mW power	Unique Cells found		
Corr. cutoff	>0.1	>0.3	>0.5
Ideal (8117 total)	446	363	258
Ideal & not CNMF	202	141	53
Ideal & not Suite2p	240	171	72
Ideal & not PCA/ICA	302	232	130
CNMF & not Ideal	0	0	1
Suite2p & not Ideal	0	0	0
PCA/ICA & not Ideal	0	0	0

Supplementary Table 17: Somatic component recovery via automated calcium imaging video segmentation as applied to simulated data generated from NAOMi with 80 mW laser power.

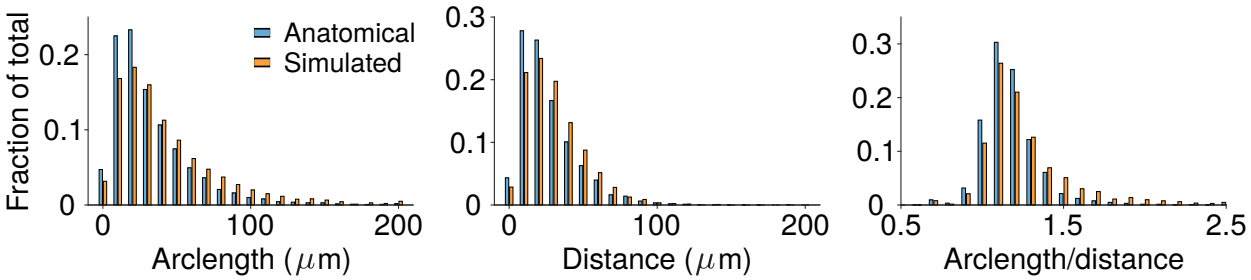

Supplementary Figure 2: Histograms comparing the lengths of vasculature between the NAOMi simulation and observed distributions in data from [106].

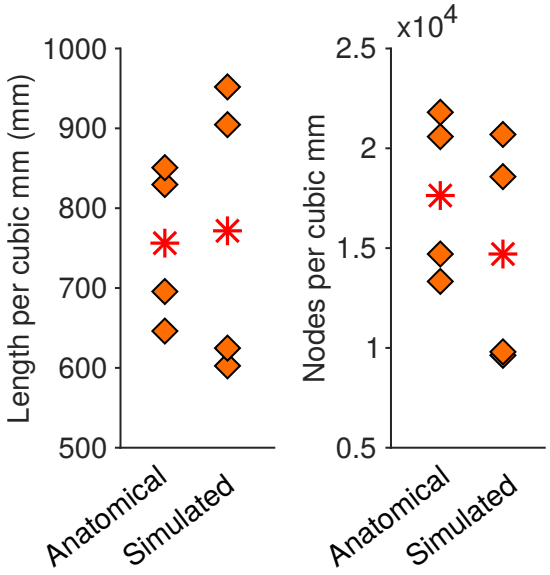

Supplementary Figure 3: Comparison of overall length of the vasculature and the number of vasculature nodes within a cubic mm volume. Comparisons are to observed distributions in data from [106].

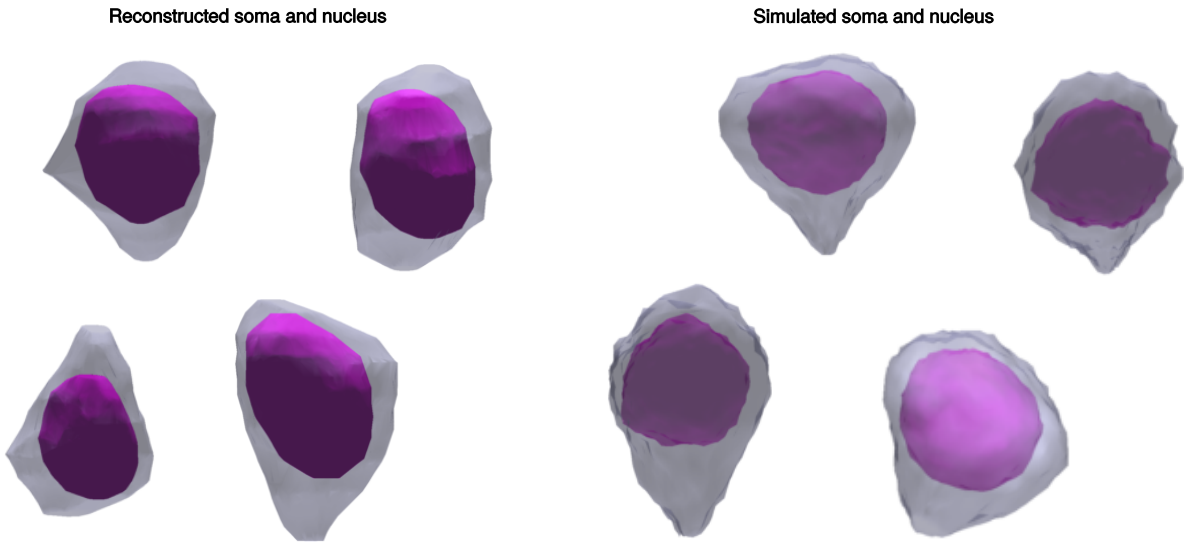

Supplementary Figure 4: Examples of measured and simulated somas. Both measured somas (left) and simulated somas (right) have a bumpy cell wall with one end exhibiting the cone-shaped tightening characteristic of pyramidal cells. The nuclei of both sets of somas (blue shape inside of the red shape) are shrunken and smoothed versions of the exterior cell wall.

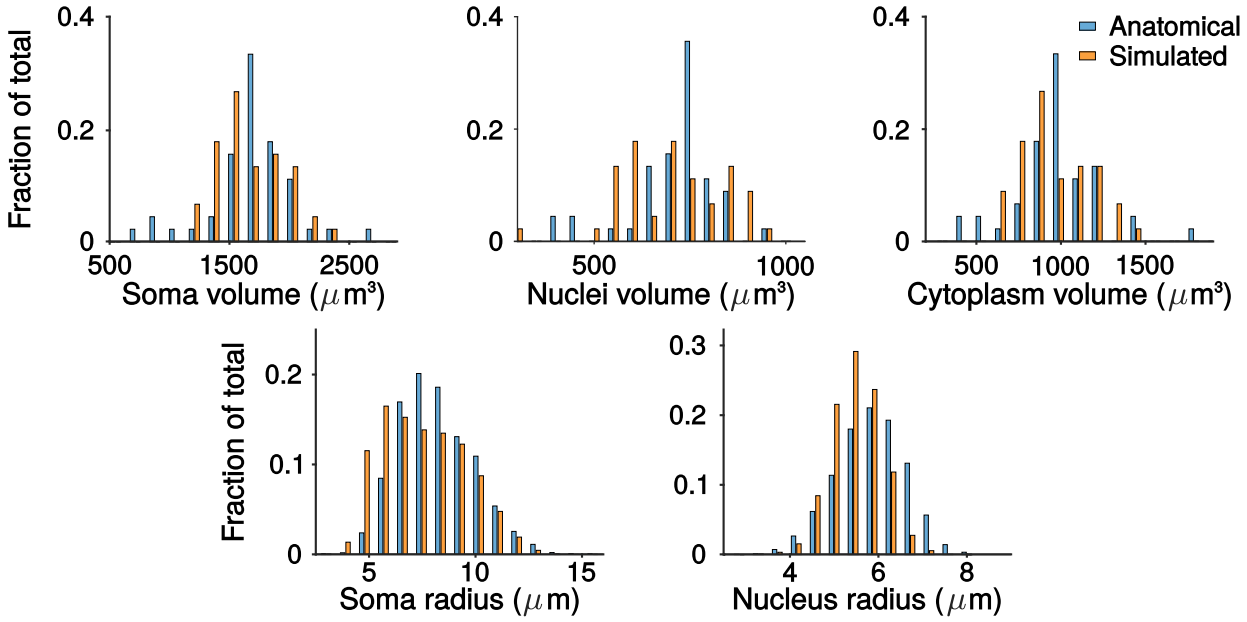

Supplementary Figure 5: Histogram comparing simulated somas with measured anatomy.

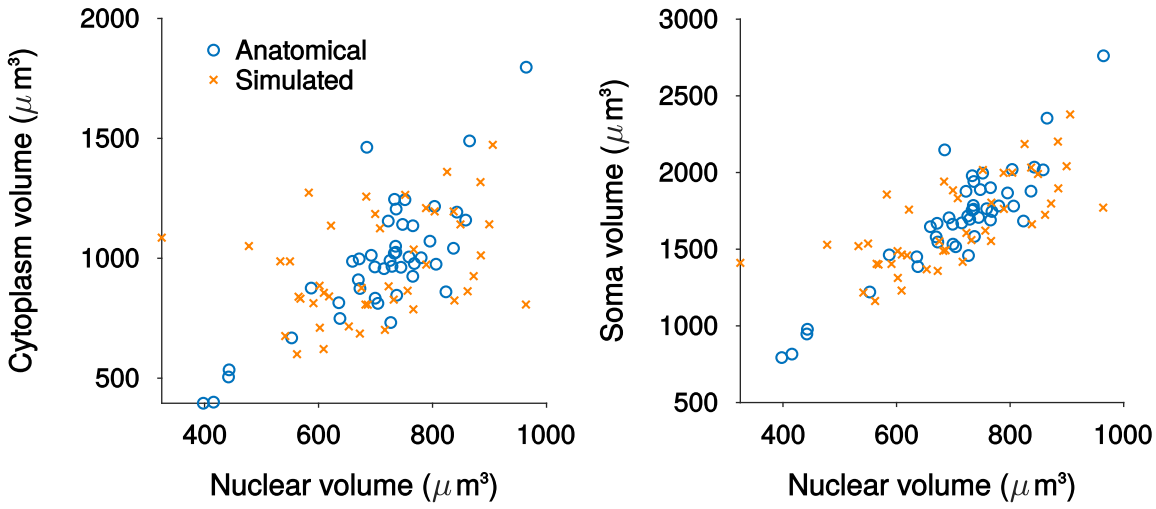

Supplementary Figure 6: Scatter plots comparing the nucleus, soma and cytoplasm volumes for simulated neurons with measured anatomy from EM reconstructions.

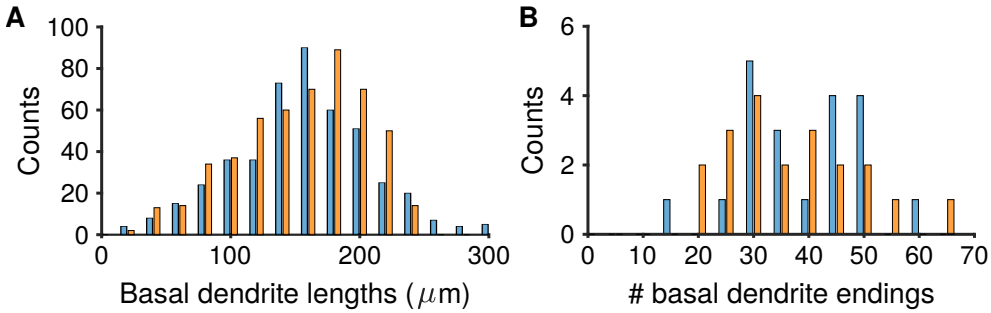

Supplementary Figure 7: A: Histogram of total basal dendrite length per cell from measured [60] and simulated data. B: Histogram of total number of basal dendrite endings

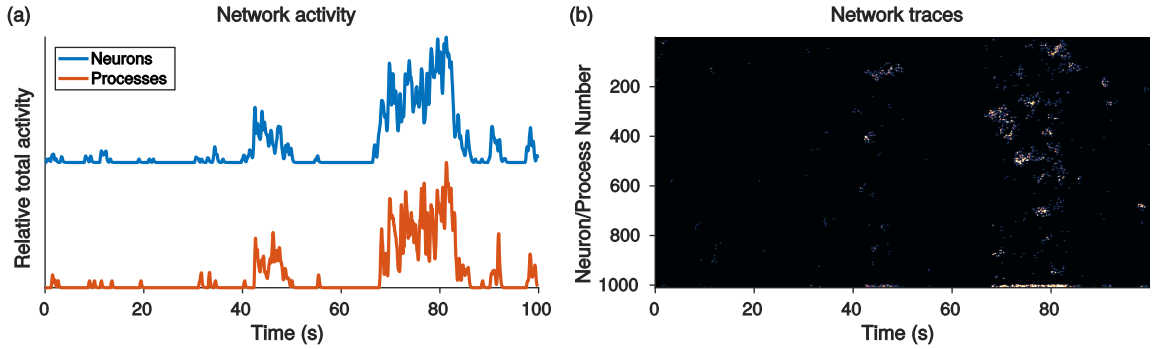

Supplementary Figure 8: Example of a Hawkes point-process. (a) The total activity of the network is correlated with the total activity in the background processes. (b) The Hawkes process gives the network- and single neuron- bursting statistics common in many neural activity recordings.

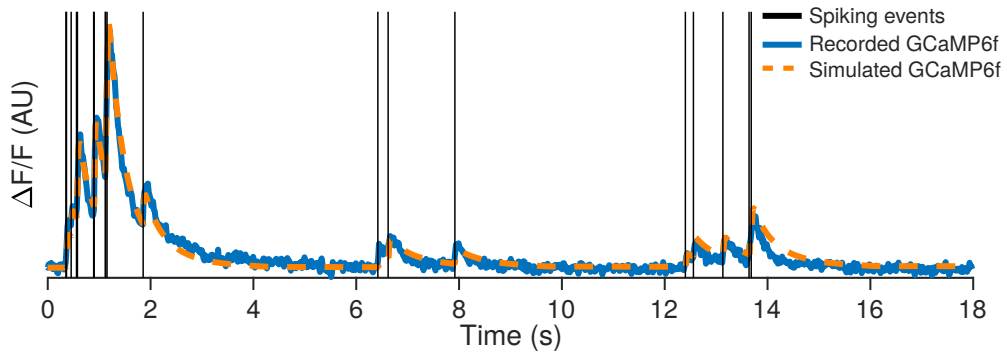

Supplementary Figure 9: Simultaneously recorded spikes and two-photon fluorescence time-course [46] along with the estimated fluorescence timecourse using a forward model of calcium response.

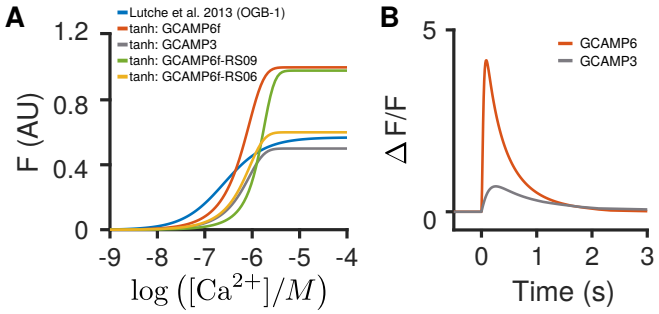

Supplementary Figure 10: A: Example hill plots that can be used in the fluorescence simulation (relating calcium concentration to $\Delta F/F$). The height and slope dictate the saturation and decay behavior. These curves were to the indicators in [71], using the parameters supplied therein. B: Example $\Delta F/F$ behavior for GcAMP6f and GcAMP6s in response to a ten-spike burst.

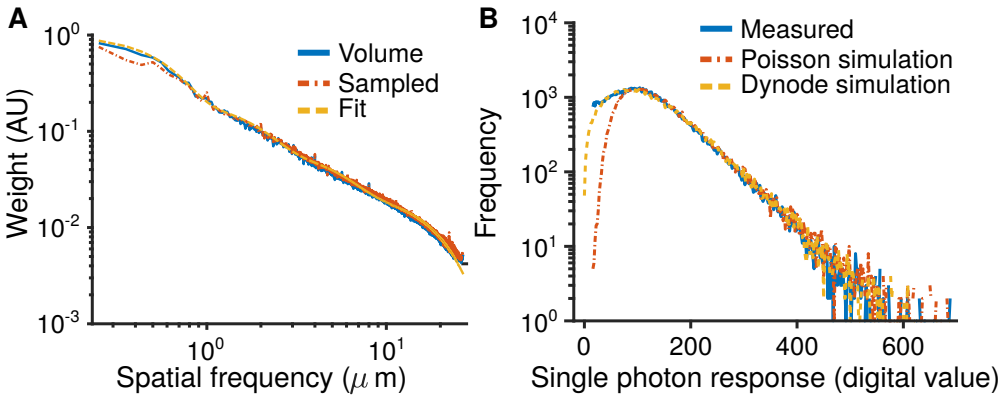

Supplementary Figure 11: A: Spatial frequency weights of an EM volume of mouse visual cortex, the fit to a Gaussian mixture model (GMM), and weights from a 3D Gaussian process sampling using the GMM. B: Measured PMT single photon response digital count distribution as compared to a Poisson amplification model or a dynode amplification model.

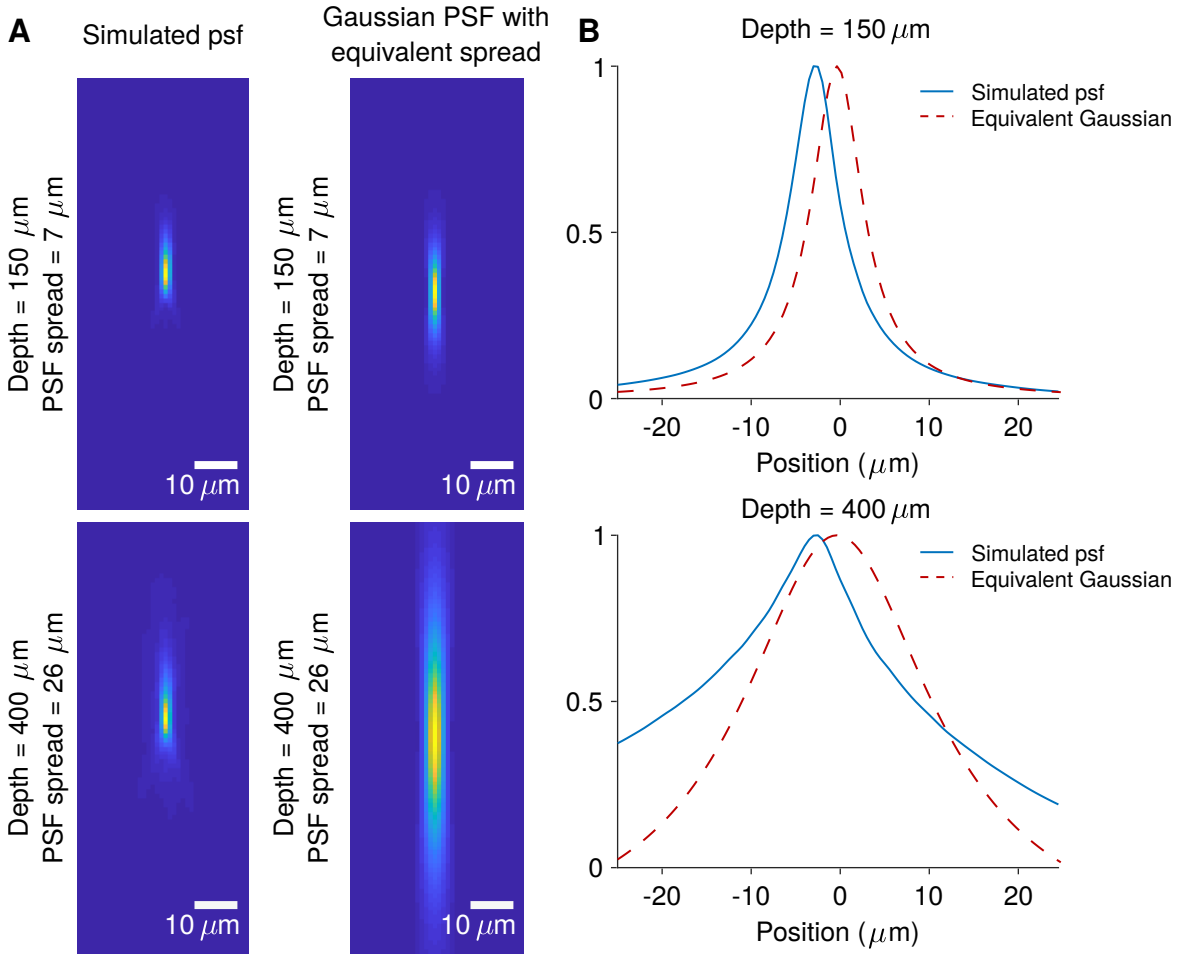

Supplementary Figure 12: A: Simulated NAOMi PSF distributions at 150 μm and 400 μm depths. The full-width half-maximum intensity estimates for these distributions are 7 μm and 26 μm respectively. Simulated two-photon Gaussian beam PSF with 7 μm and 26 μm FWHM. While the shallow volume axial distribution mostly reflects the Gaussian beam PSF, the deeper volume PSF cannot be accurately described with a simple Gaussian beam. Similarly, a Gaussian beam aberrated only with spherical aberration also cannot accurately describe the full PSF (not shown). B: Corresponding cross-sections of the PSFs depicted in panel A.

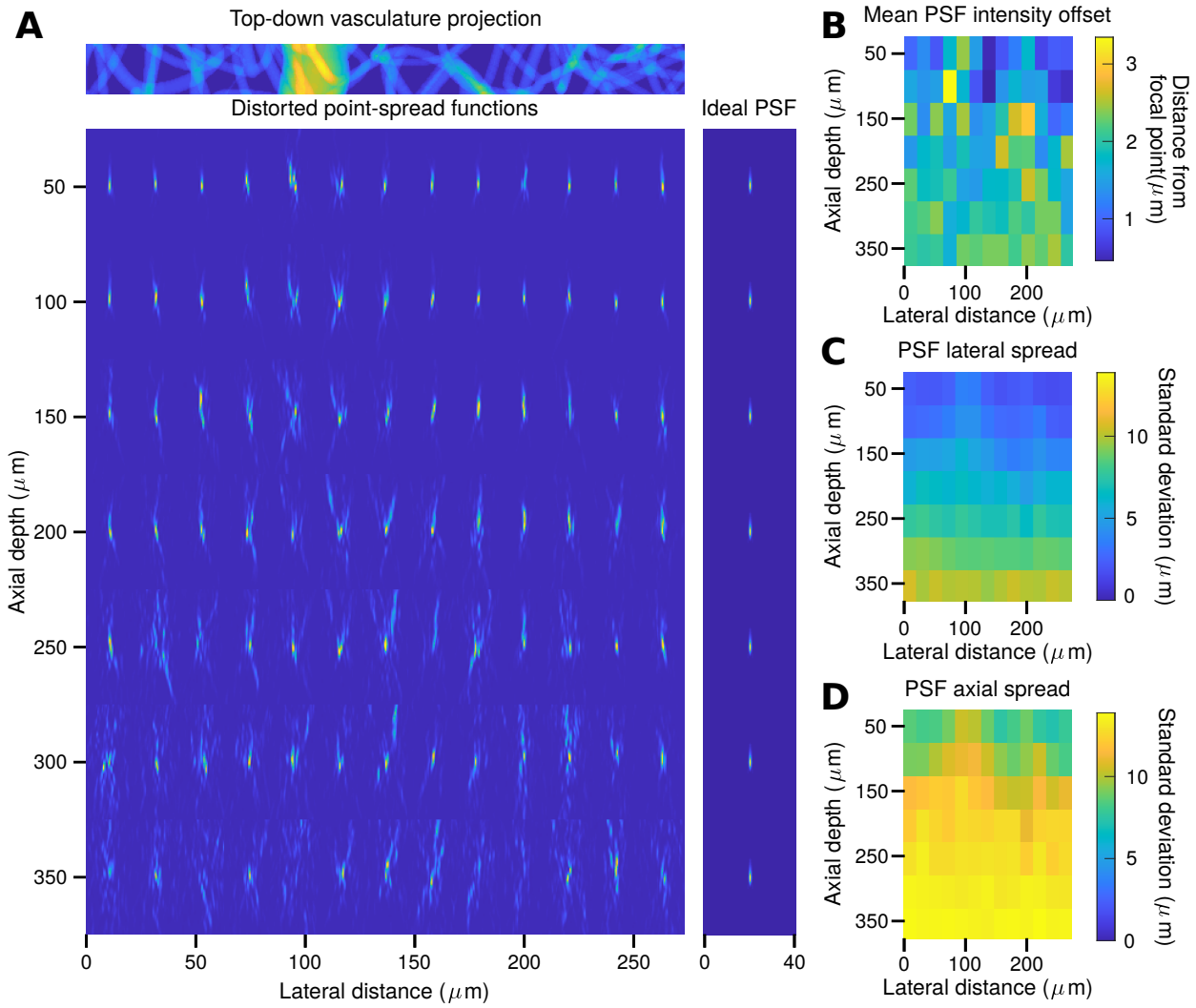

Supplementary Figure 13: Simulated propagation of a point-spread function through layers of diffusing tissue using NAOMi. A: (Top) Axial projection of the vasculature in the simulated tissue. Note the large surface vessel at the 100 μm mark. (Bottom) Simulated PSFs equally spaced across two $\approx$2000 μm cross sections of tissue, sampled at 10 μm spacing. B: Quantitative plot showing the distance of the mean intensity position from the intended focal point of the PSF as a function of location in the volume slice. There is a slight increase in displacement deeper in the volume. C: Comparison of lateral spread (lateral standard deviation of the PSF intensity) as a function of location in the volume. Deeper tissue has a pronounced increase in lateral spread. D: Comparison of axial spread (axial standard deviation of the PSF intensity) as a function of location in the volume. Axial spread grows much faster than lateral spread, in particular in the region directly beneath the blood vessel.

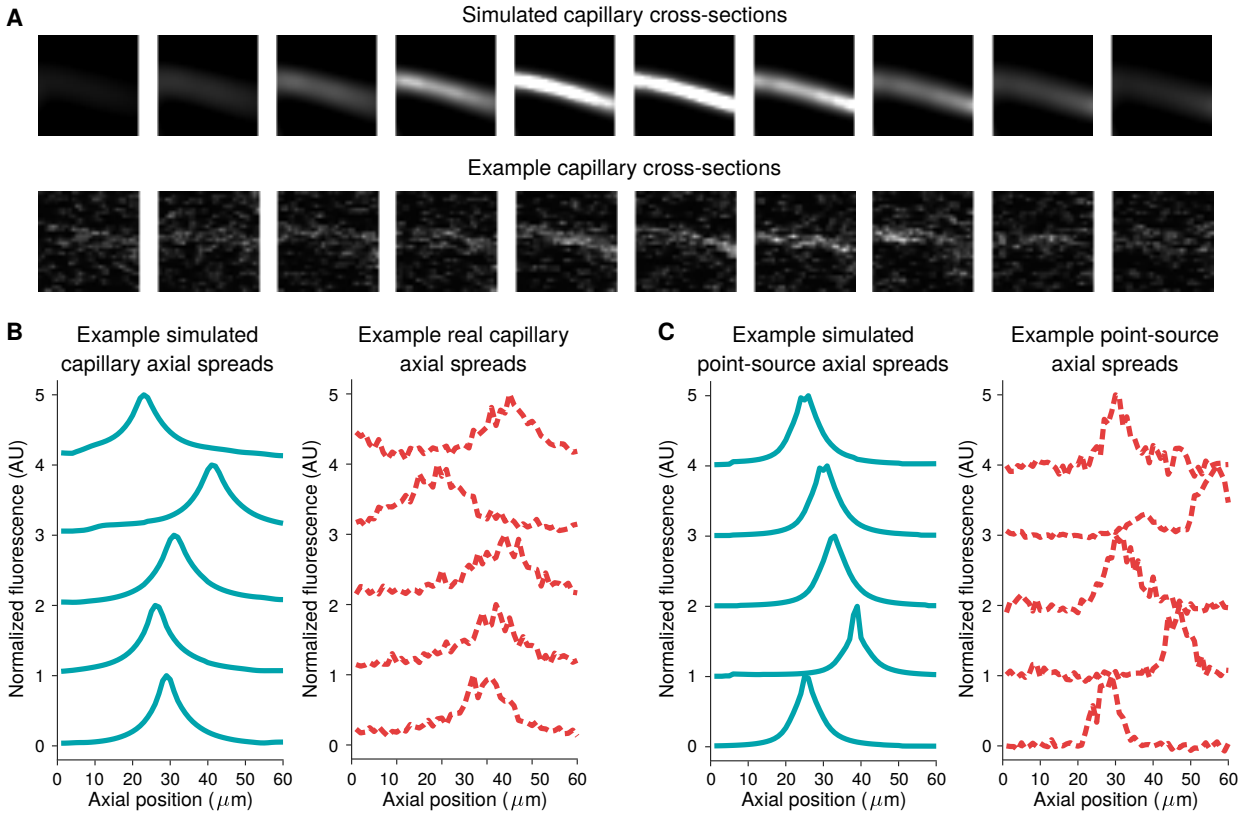

Supplementary Figure 14: A: Example simulated and real capillaries with 2 μm separation between successive images. The width and axial extent of these structures can be used to give an upper bound of and an approximate estimate of the PSF axial spread. Similarly, point sources (not shown) may be used to offer a direct measurement of the PSF in the sample. B: Example distributions for simulated and real axial spread for capillaries at approximately 330 μm in depth. Tissue aberrations increase the spread of the PSF to several times the unaffected width. The estimated spread of the simulated capillaries are 12.65$\pm$3.60 μm (axial) and 5.33$\pm$0.65 μm (lateral) and the real capillaries are 13.99$\pm$2.29 μm (axial) and 5.60$\pm$0.41 (lateral). These result in an estimated PSF axial spread of 9.98$\pm$3.8 μm (simulated) and 11.19$\pm$2.31 μm (real). The simulated estimate is comparable to the known axial PSF spread of 9.13 μm. Axial positions are referenced to a position at a depth of 300 μm. C: Similar example distributions for simulated and real axial spread for point sources at approximately 330 μm in depth. The estimated axial spread of the simulated point sources are 7.15$\pm$2.40 μm and the real point sources are 8.64$\pm$1.34 μm. The estimated axial spread of the point sources are lower than the actual value due to the coarse spatial sampling used. Axial positions are referenced to a position at a depth of 300 μm. All numbers given as mean and standard deviation.

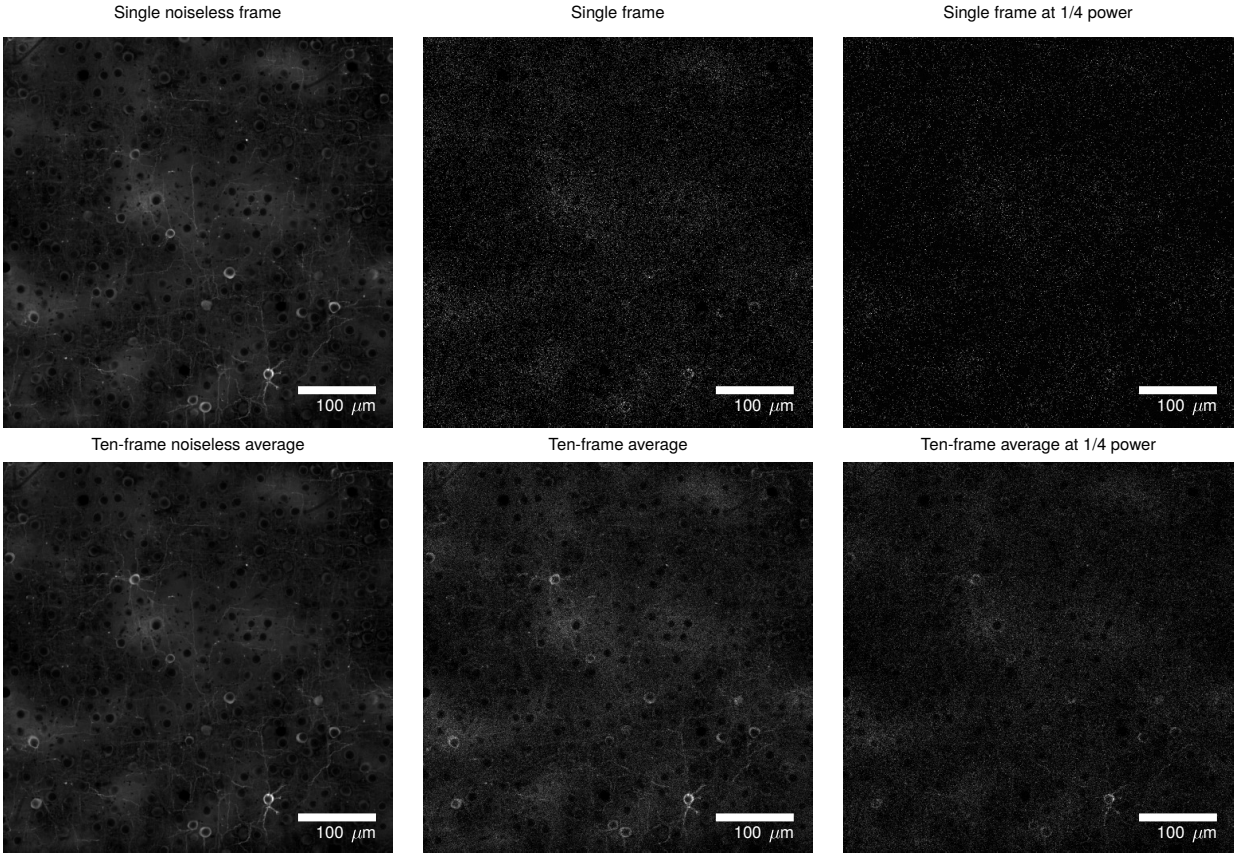

Supplementary Figure 15: Example frames showing the effect of reducing the power of the scanning PSF.

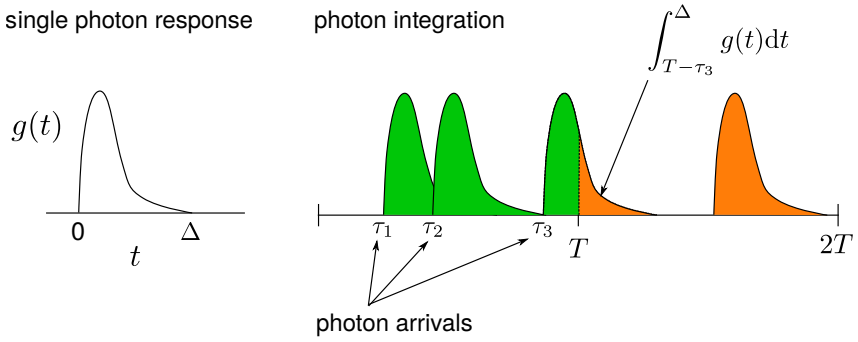

Supplementary Figure 16: Bleed-through of photon responses during TPM electronic analog-to-digital conversion. Left: A single photon causes a response in the electronics that persists over a time frame Δ. Right: any photons that arrive within Δ of the end of the sampling period cutoff (every T seconds) have responses that are partially integrated into the current sample (green) and partially integrated into the next sample (orange).

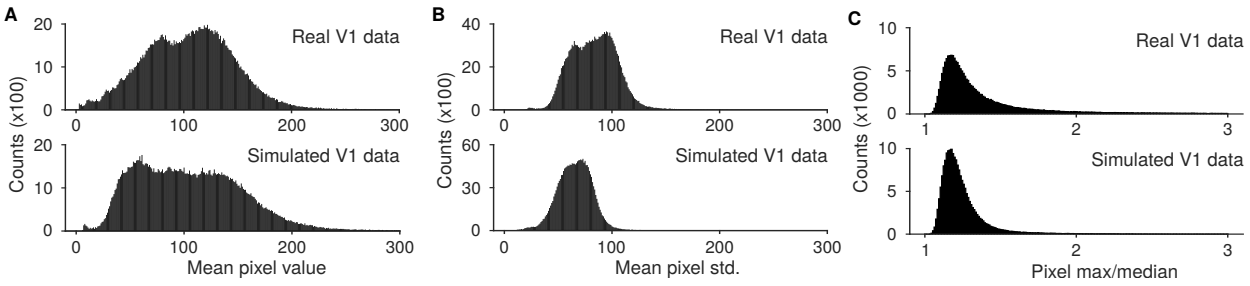

Supplementary Figure 17: A: Histogram of values in the mean image over 20000 frames for both real and simulated V1 data. B: Histogram of standard deviations across the FOV over 2000 frames for both real and simulated V1 data. C: Histogram of the ratio of the maximum value to the median value (approximate estimte of activity) across all pixels in the FOV, calculated over 20000 frames.

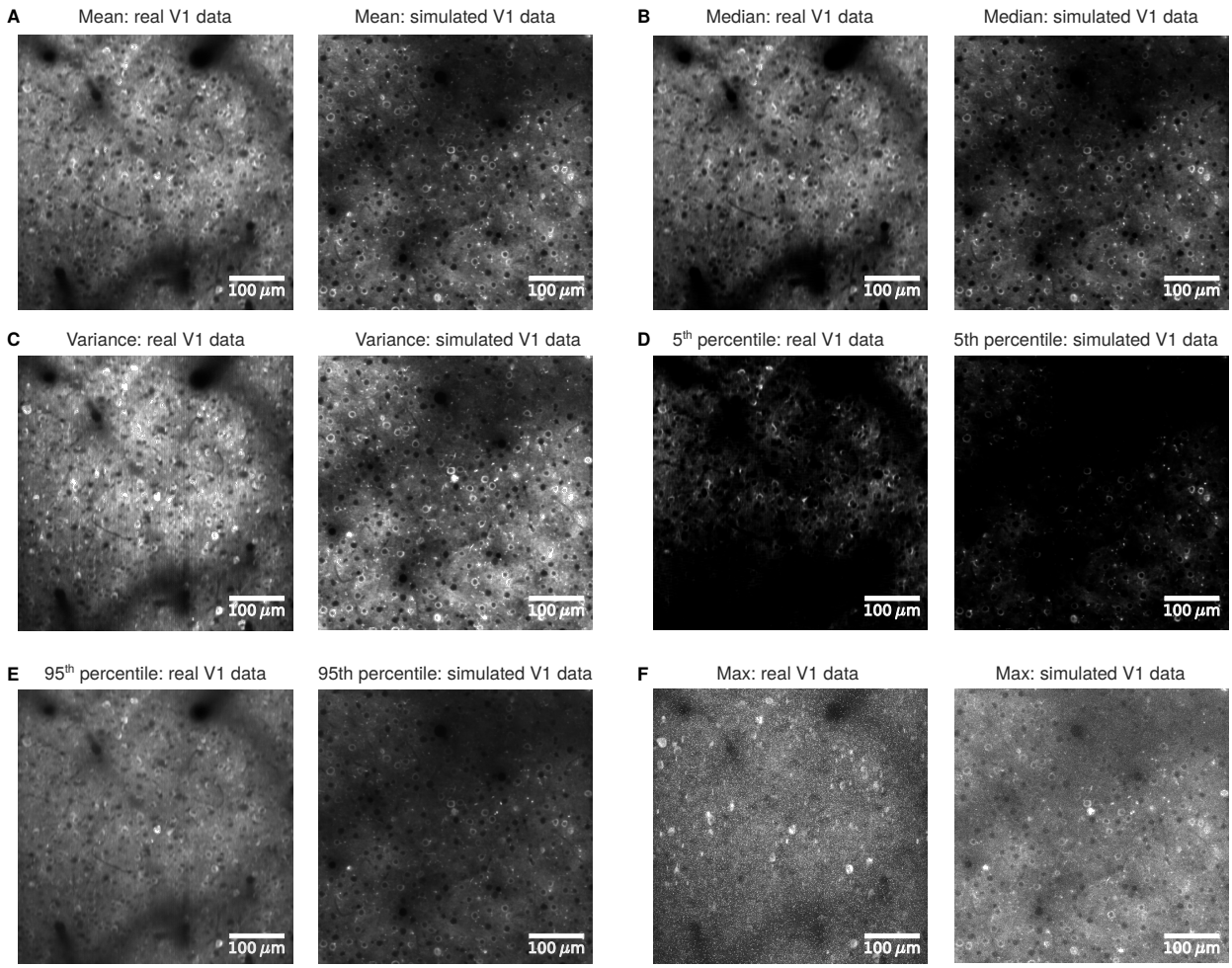

Supplementary Figure 18: Comparisons of different projection images for real V1 and simulated V1 data. A: Mean image (temporal mean of each pixel). B: Median image (temporal median of each pixel). C: Variance image (temporal variance of each pixel). D: 5^{th} percentile image (5^{th} percentile of each pixel's time trace). E: 95^{th} percentile image (95^{th} percentile of each pixel's time trace). f: Max image (temporal max of each pixel).

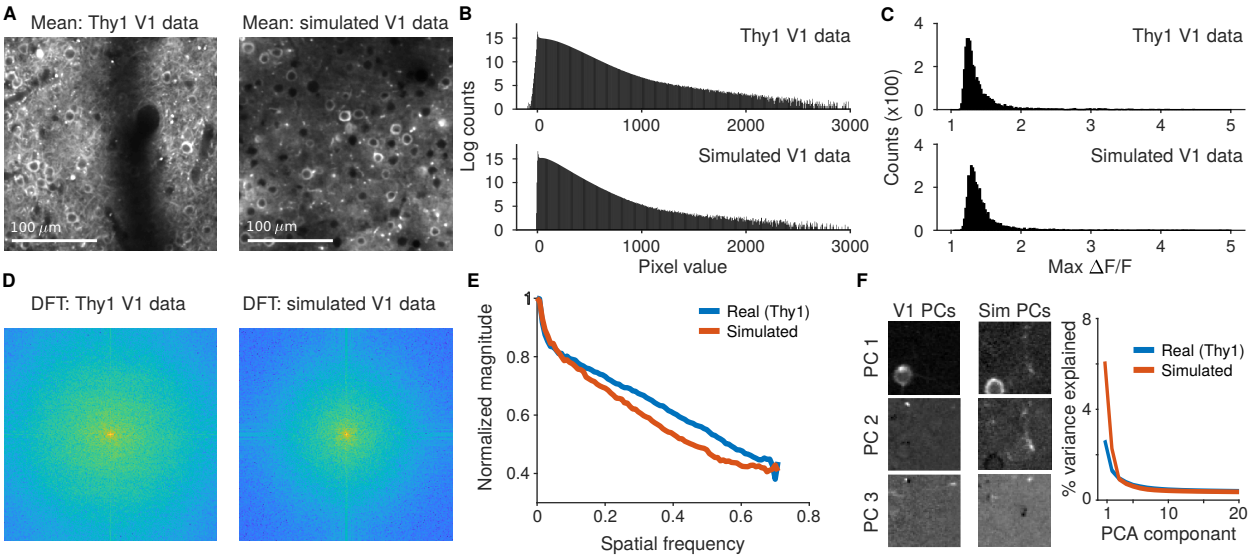

Supplementary Figure 19: Comparison of simulated data to recordings of Thy1 GP5.3 mouse V1 L2/3 using GCaMP6f. A: The mean image for mouse V1 recordings and simulated data. B: Pixel value distributions across the full videos display bimodal peaks and a right log-linear tail. C: Distribution of the maximum $\Delta F/F$ values across all pixels in the FOV match between the simulated and Thy1 V1 data. D: The spatial frequency content in the mean simulated image captures the qualities of the Thy1 data. Both the spread of frequencies and the tendency for high-frequency components in the fast- and slow- scan directions that result from line-by-line motion and pixel bleed-through are captured. E: The overall contributions at different spatial frequencies to the mean activity matches between the recording and simulation. F: Principal component decompositions for both the Thy1 and simulated data exhibit similar decays in the variance explained per component. The resulting spatial principal components are qualitatively similar.

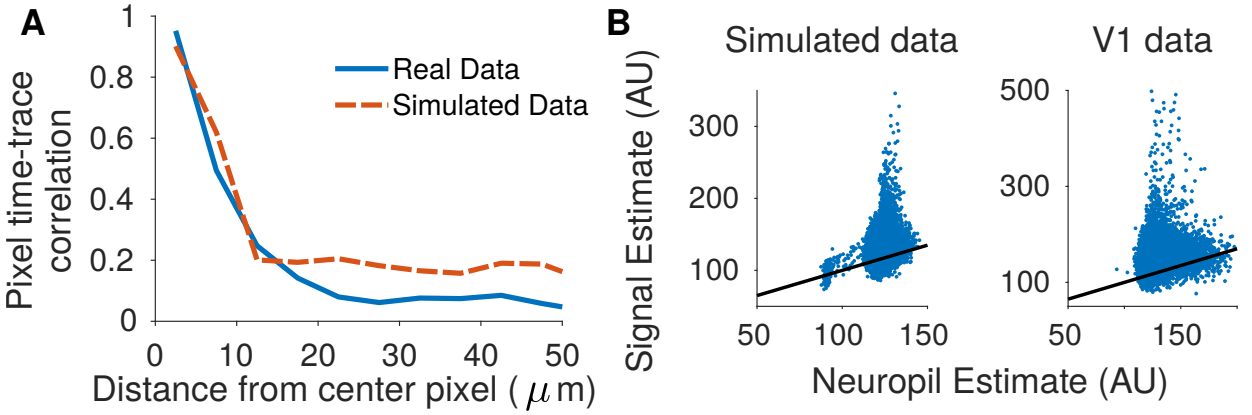

Supplementary Figure 20: Correlation of pixels at a distance from found the time-course of components found using CNMF shows a fall-off consistent between NAOMi simulations and real data. Correlations are highest near the center of the cell and drop off rapidly at a distance, represent neuropil correlations. The black line has a slope of 0.7, indicating general agreement with past observations [34]

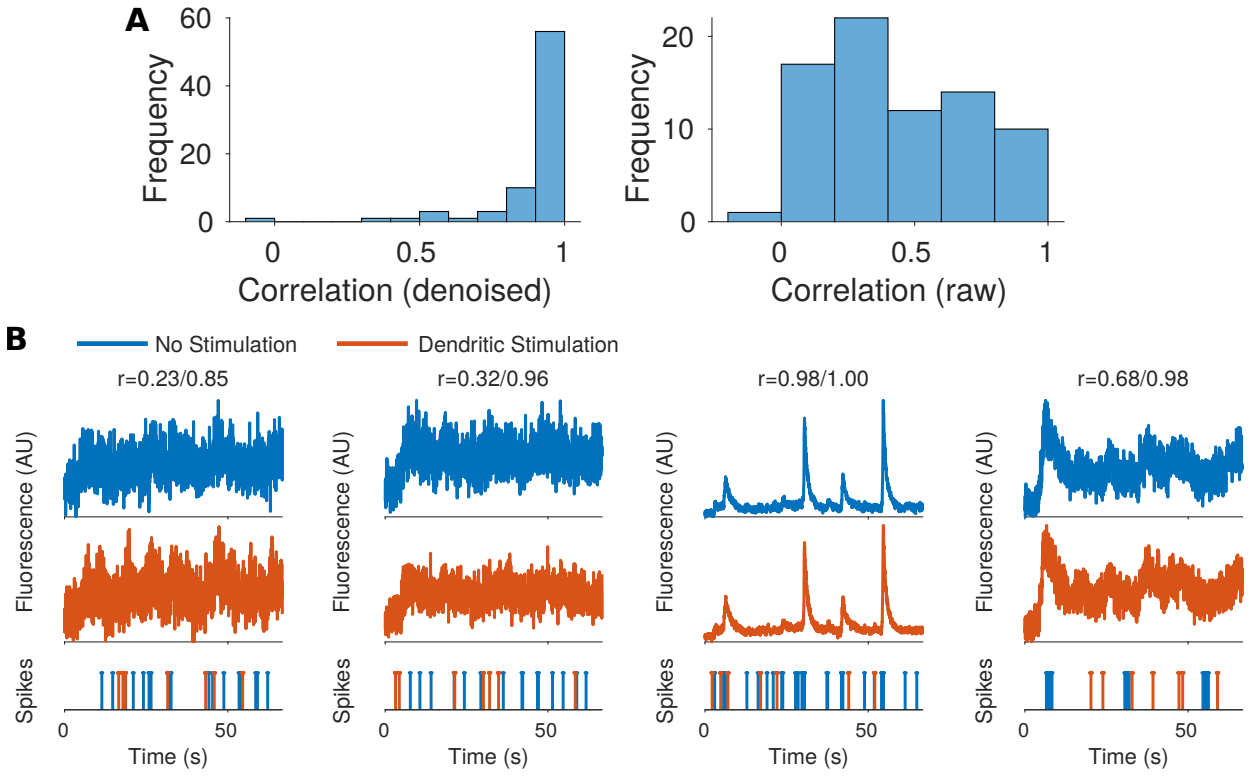

Supplementary Figure 21: Robustness of time-traces to dendritic stimulation. A: Histograms of the correlation coefficients between the ideal traces estimated from the same volume and additional dendritic spikes artificially introduced into the activity for one of the two simulations. Both the raw correlations (right) and the correlation between denoised time-traces (using standard wavelet-based denoising) show that the dendritic spikes do not significantly perturb the inferred traces. B: Example traces with (orange) and without (blue) added dendritic stimulation. Correlation values (raw/denoised) are given above. The spike trains below show the original spike train in blue and the added dendritic spikes in orange that only effect the orange trace above them.

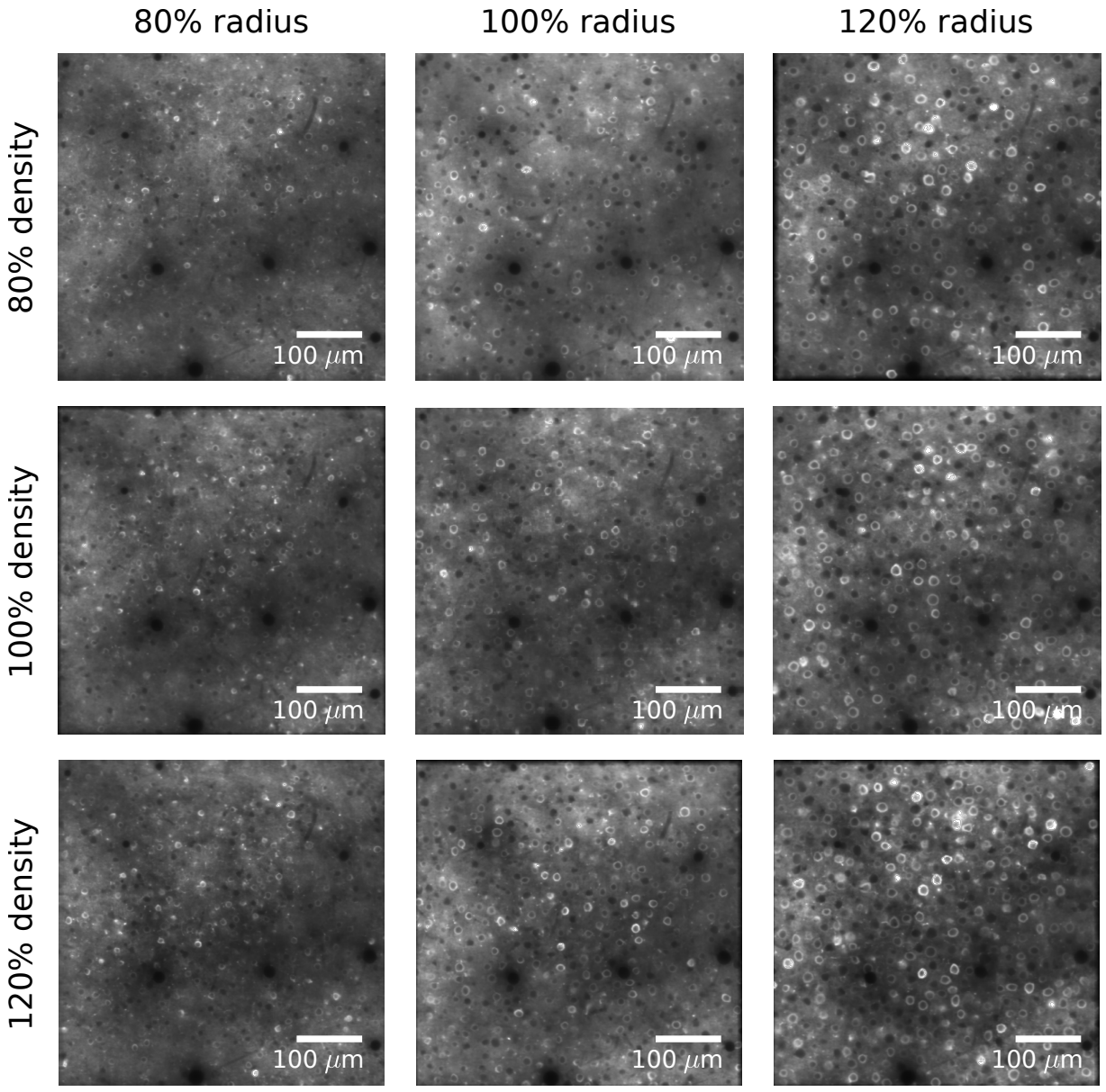

Supplementary Figure 22: Varying the cell size and density in the NAOMi simulation can change the generated video properties. Shown here are the mean images of videos generated by varying the cell size and density by $\pm 20\%$. We note that changing the cell size has a much larger impact on the qualitative properties of the observed mean images.

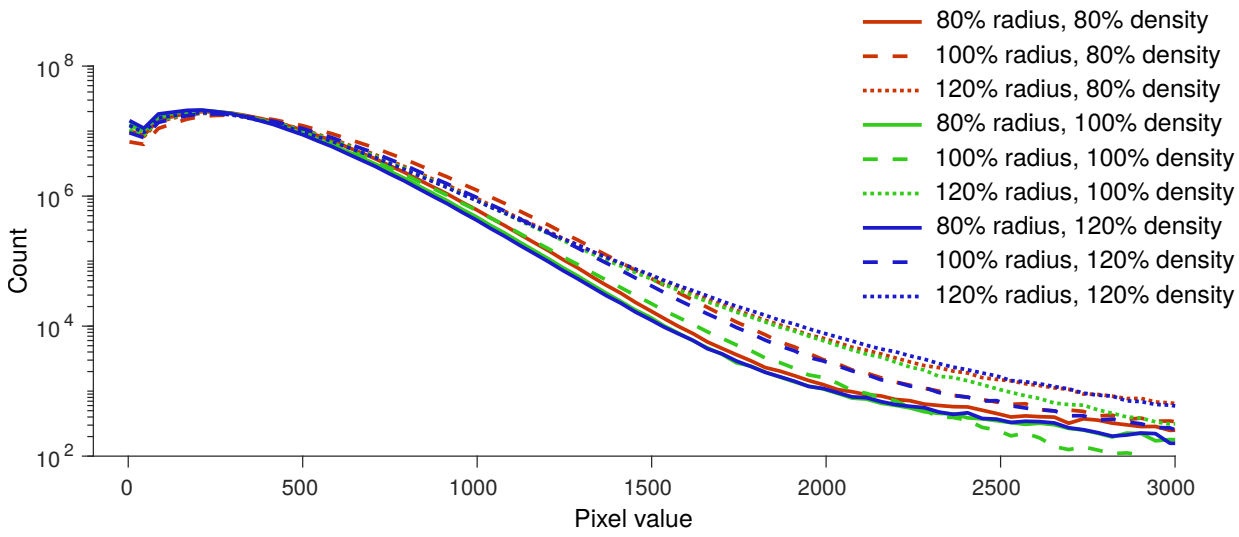

Supplementary Figure 23: Varying the cell size and density in the NAOMi simulation can change the generated video properties. Shown here are the histograms of pixel values for videos generated by varying the cell size and density by ±20%. Histograms for specific cell sizes tend to cluster together, for example videos with cells enlarged by 20% have heavier tails while cells shrunk by 80% have tighter tails. . Changes in cell density do not seem to have nearly as much of an impact, for example the distributions of values across all densities for videos with 20% larger cells are nearly identical.

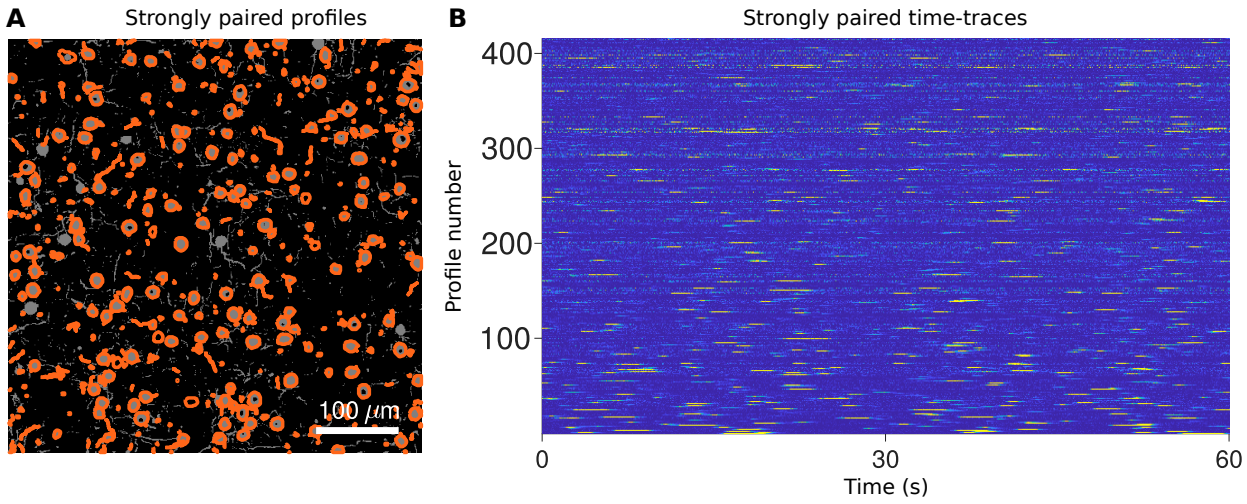

Supplementary Figure 24: Results of using the ideal spatial components to de-mix the simulated TPM video with frame-by-frame least-squares.

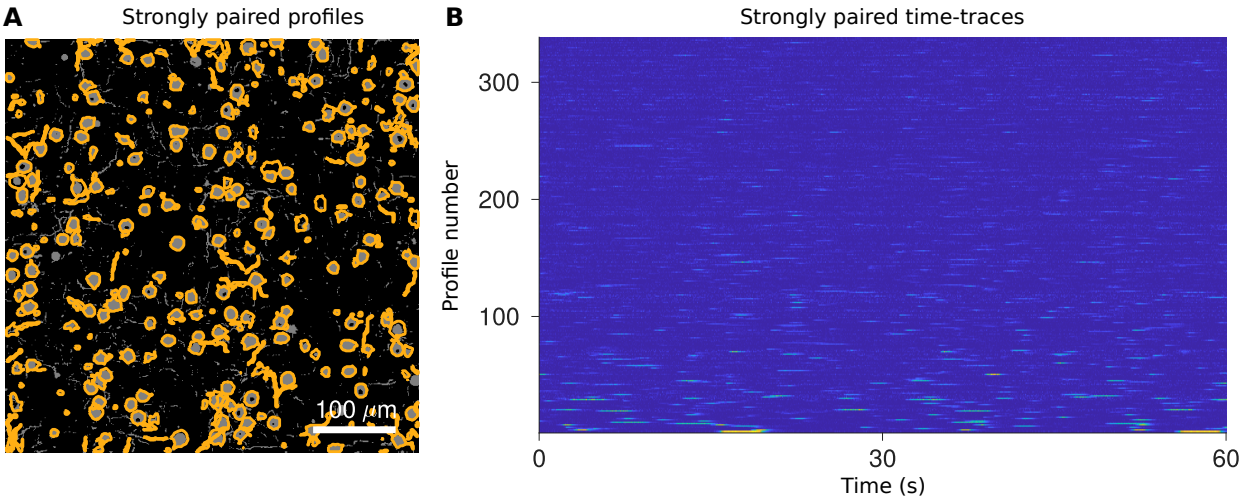

Supplementary Figure 25: Results of using CNMF to analyze the simulated TPM video.

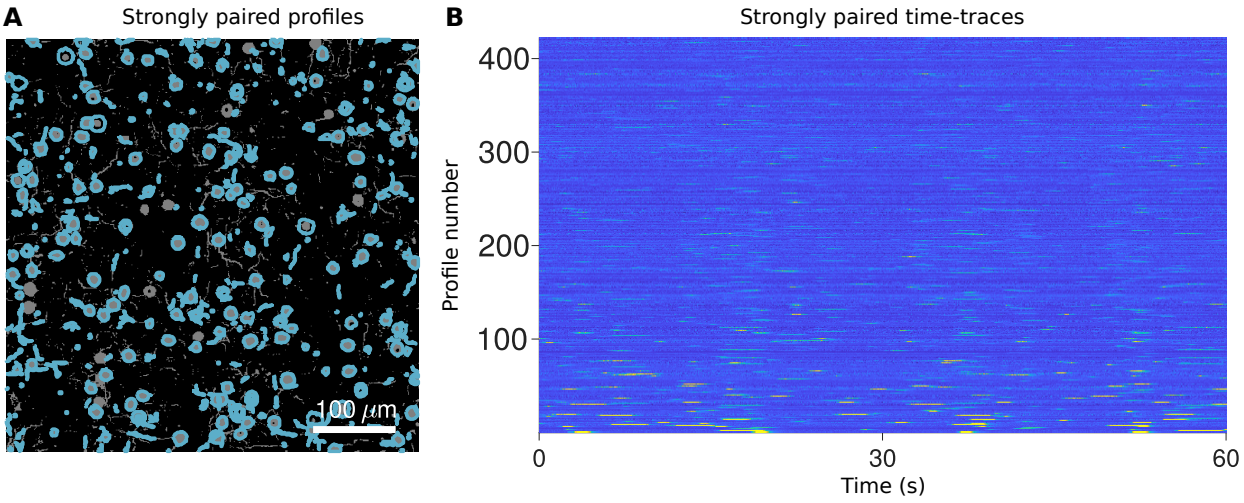

Supplementary Figure 26: Results of using Suite2p to analyze the simulated TPM video.

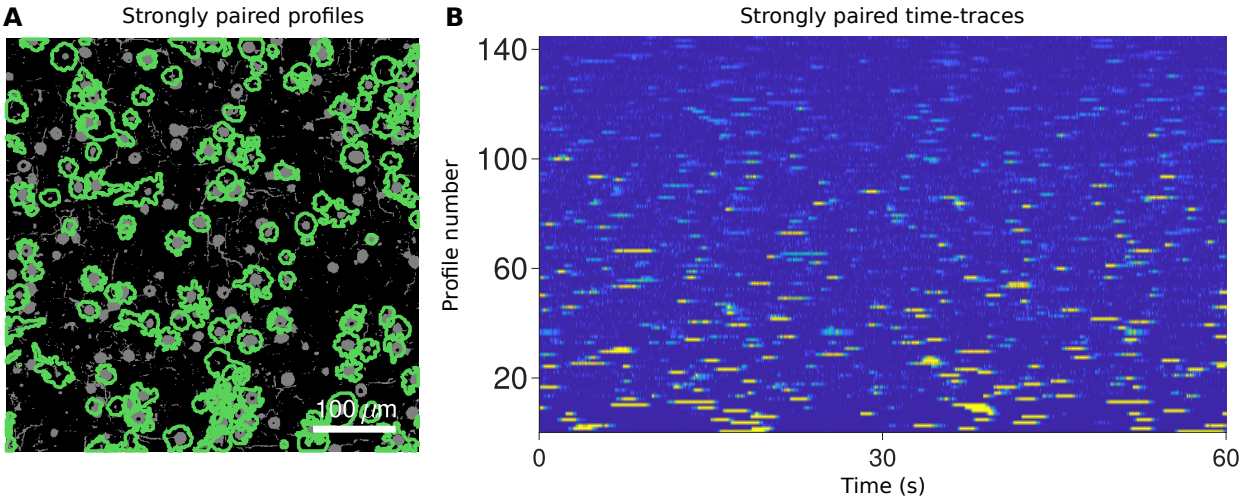

Supplementary Figure 27: Results of using the PCA/ICA to analyze the simulated TPM video.

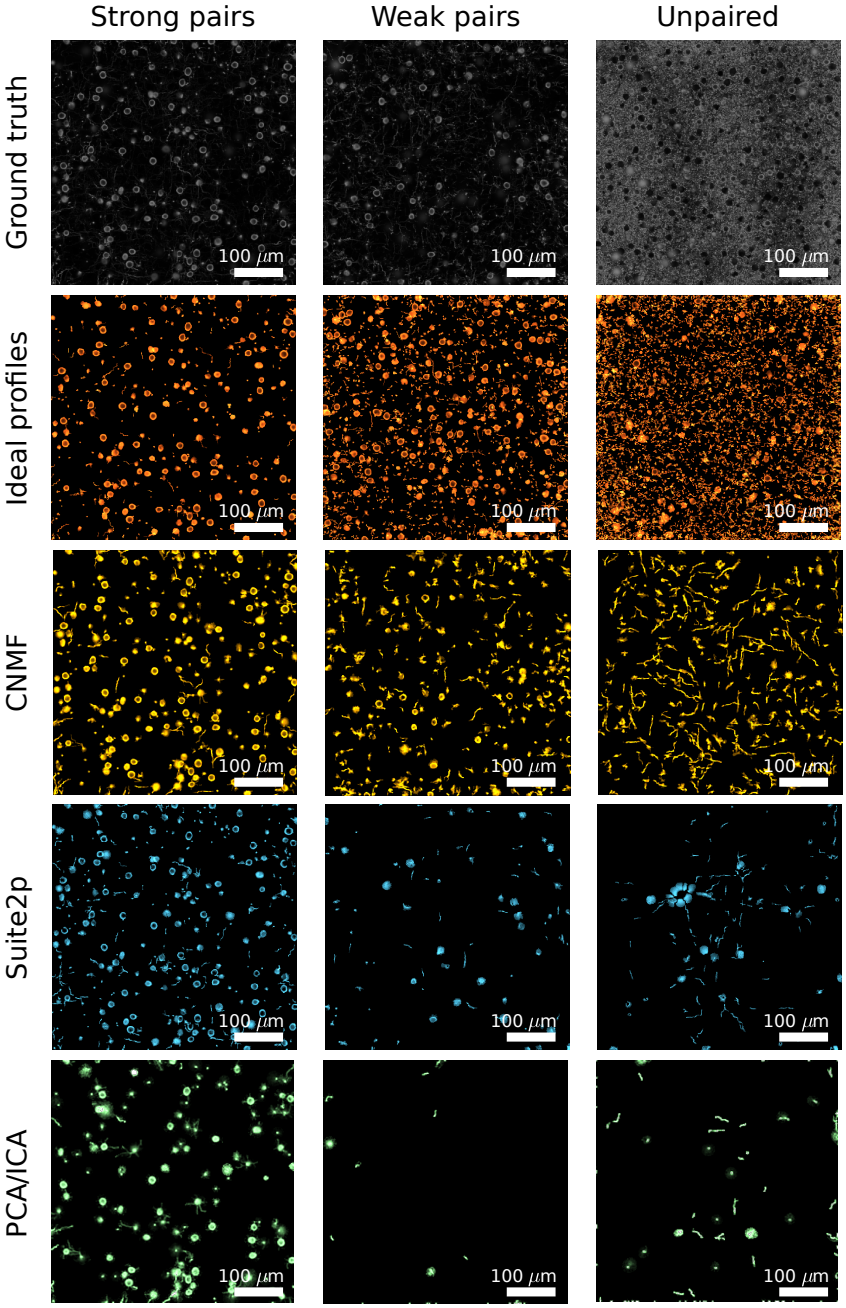

Supplementary Figure 28: Profile shapes for strongly paired profiles ($\rho > 0.5$; left column), weakly paired profiles ($0.1 < \rho < 0.5$; middle column) and unpaired profiles ($\rho < 0.1$; right column). Most cells (top row), were unpaired. Paired cells tended to be found via their somatic signal. CNMF (second row) tended to find the most profiles and matched the most cells. CNMF, however, also found the most false-positives, which tended to be dendritic shapes. Suite2p (third row) found both fewer cells and fewer false positives. PCA/ICA had the lowest number of found cells but still had a significant number of false positives.

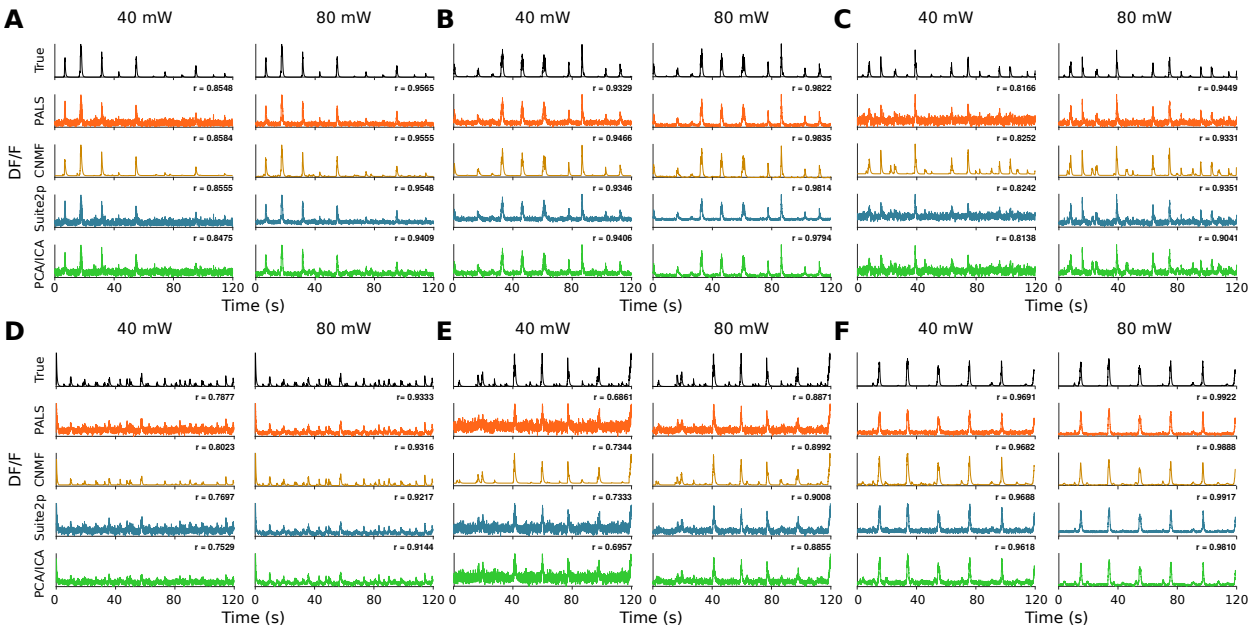

Supplementary Figure 29: Examples of strongly paired time-traces in simulations using 0.6 NA Gaussian beams 40 mW and 80 mW power.

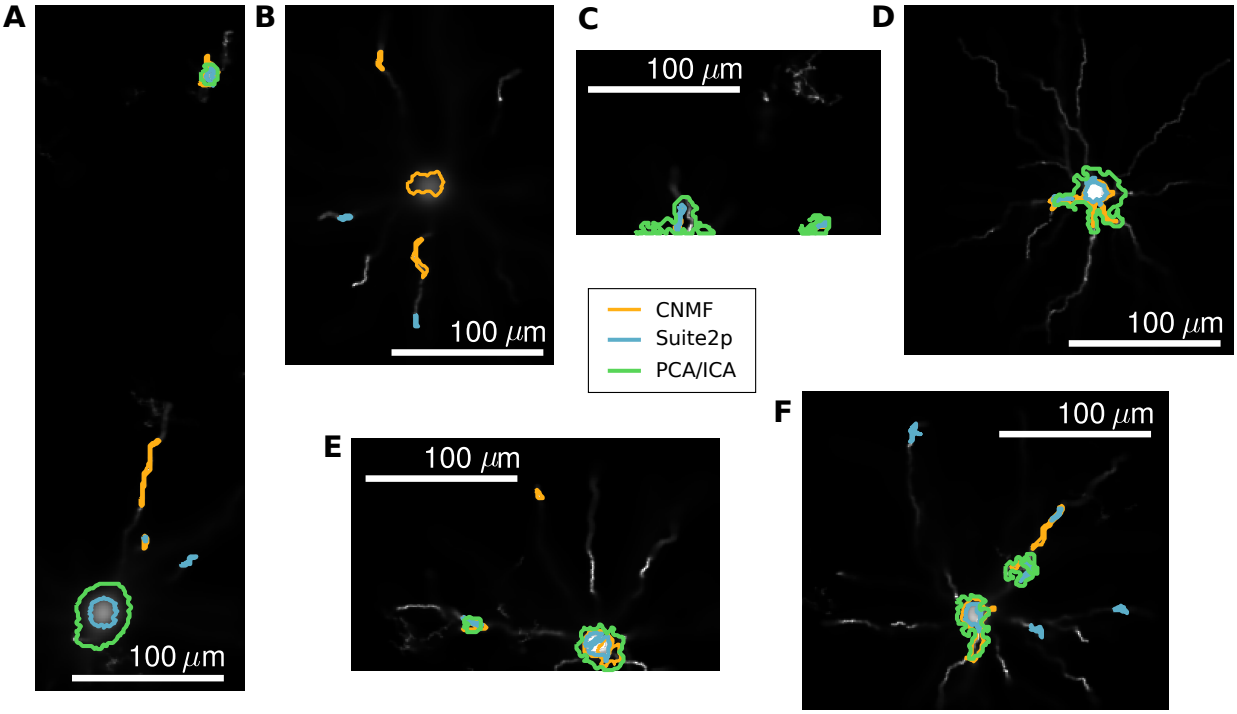

Supplementary Figure 30: Examples of cells that were found with multiplicity by one or more algorithms. A: Such cells can have profiles that are hundreds of μm away. B. More than two profiles can represent the same cell and often capture dendritic portions away from the soma. C: Such duplicity can happen when the F.O.V. cuts off a portion of the cell. D: Some examples were observed where the dendrite profile and soma profile were very close, where the profiles should have been merged. E: An example where two profiles represent the same soma and overlap. F: All three algorithms are susceptible to the multiplicity effect, proportionally to the number of profiles found.

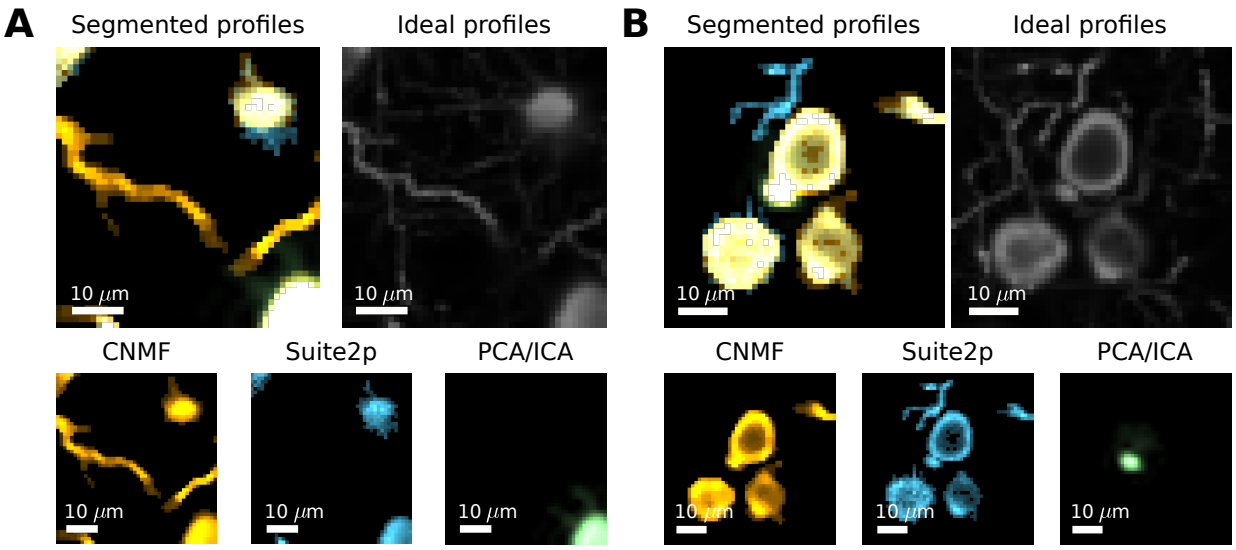

Supplementary Figure 31: Examples of finer features in the segmented profiles. Amongst the profiles found by the three different methods (CNMF in red, Suite2p in blue and PCA/ICA in green) somas were often found by multiple methods while finer features, such as dendrites were often found by only one algorithm. A: A segment containing somas found by both CNMF and Suite2p (one also found using PCA/ICA) and a dendrite found only with CNMF. B: A segment containing somas found by both CNMF and Suite2p (one also found using PCA/ICA) and a dendrite found only with Suite2p.

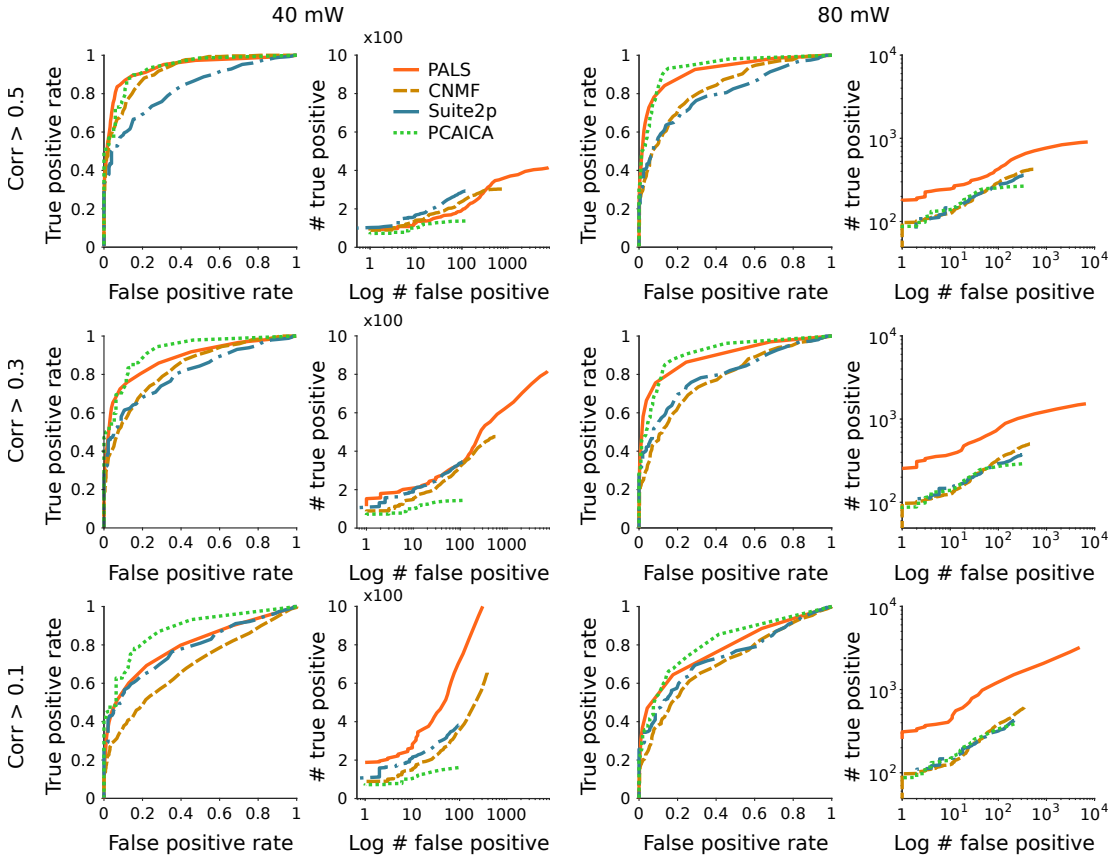

Supplementary Figure 32: Examples ROC curves at different power levels (40 mW on the left and 80 mW on the right) and with different correlation cutoffs for determining true vs. artifact sources (0.1, 0.3, and 0.5 in the three rows). Each set of curves show on the left the rates of true vs. false, as a fraction of the total number of true and artifact cells found by each algorithm, and on the right the total number of true and artifact sources.

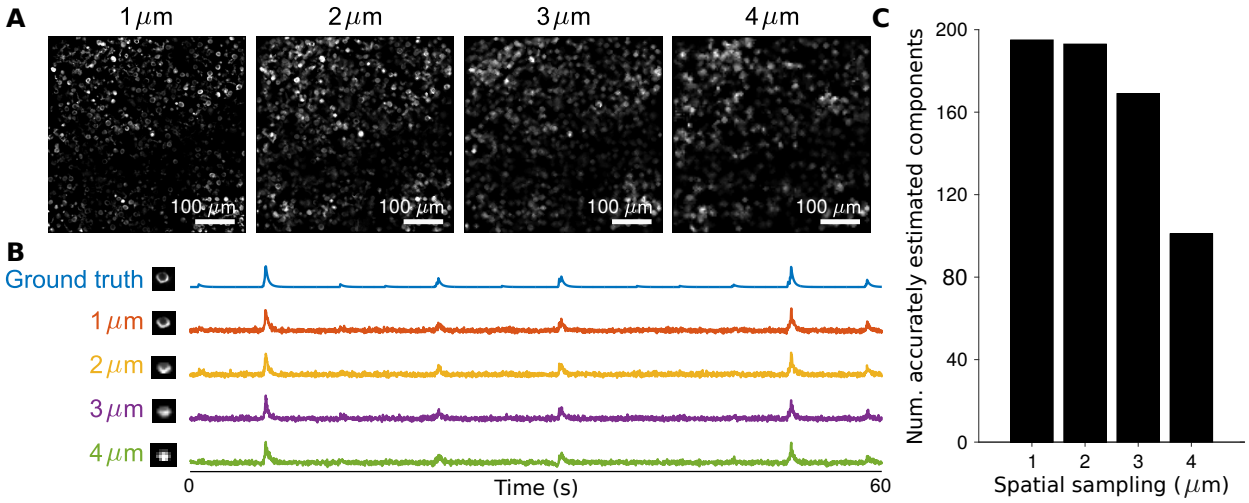

Supplementary Figure 33: Analysis of signal loss as a function of subsampling interval. A: Mean images calculated from imaging movies of the same volume and activity, taken at 1, 2, 3, and 4 μm intervals. B: Example cell spatial profile and time traces at all four image subsampling resolutions, as compared to the ground truth used to generate the data. C: Comparison of the number of cells confidently found (correlation > 0.5) at all four resolutions indicate a steep fall-off after 3 μm subsampling.

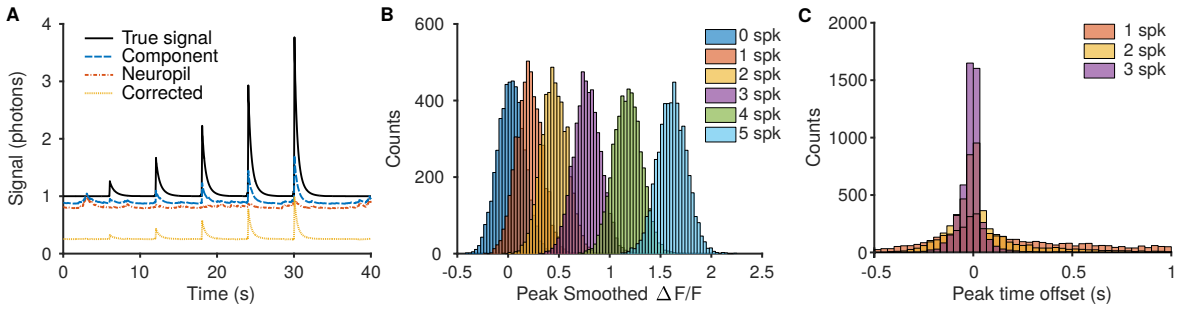

Supplementary Figure 34: Comparison of resulting ΔF/F distinguishability for bursts of different spike numbers. A: Simulations were run by generating videos with preset spiking activity that ramped up the number of spikes in each burst. Much of the error in recovered component time-traces can be attributed to insufficiently removed neuropil, and using algorithmic techniques such as in Suite2P [18] can increase the accuracy of the time traces. B: The recovered ΔF/F for larger bursts was more reliable and more separable between the different burst strengths. For example there is less overlap between the peak ΔF/F for 5- and 4-spike bursts then for 1- and 2-spike bursts. C: The peak ΔF/F offset time is also more reliable for bursts with more spikes.

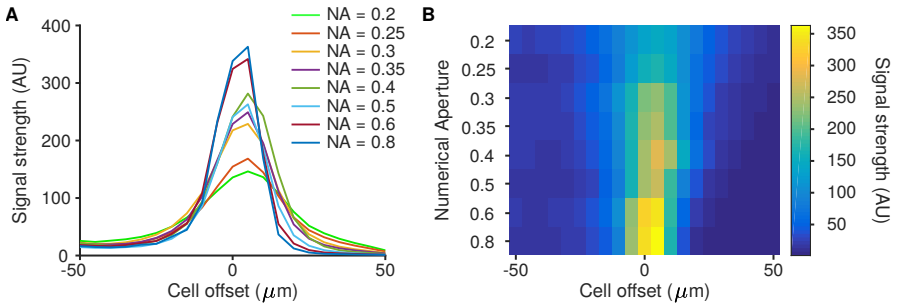

Supplementary Figure 35: Distribution of somatic signal to numerical aperture (NA) and position. Signal is defined as the square of the component somatic fluorescence divided by the baseline fluorescence and reflects the overall relative detectability of a component. A: Signal strength drops off as a function of the displacement of the cell from the peak PSF excitation. B: Same data plotted as an image to better compare spread and peak intensity of the various curves.

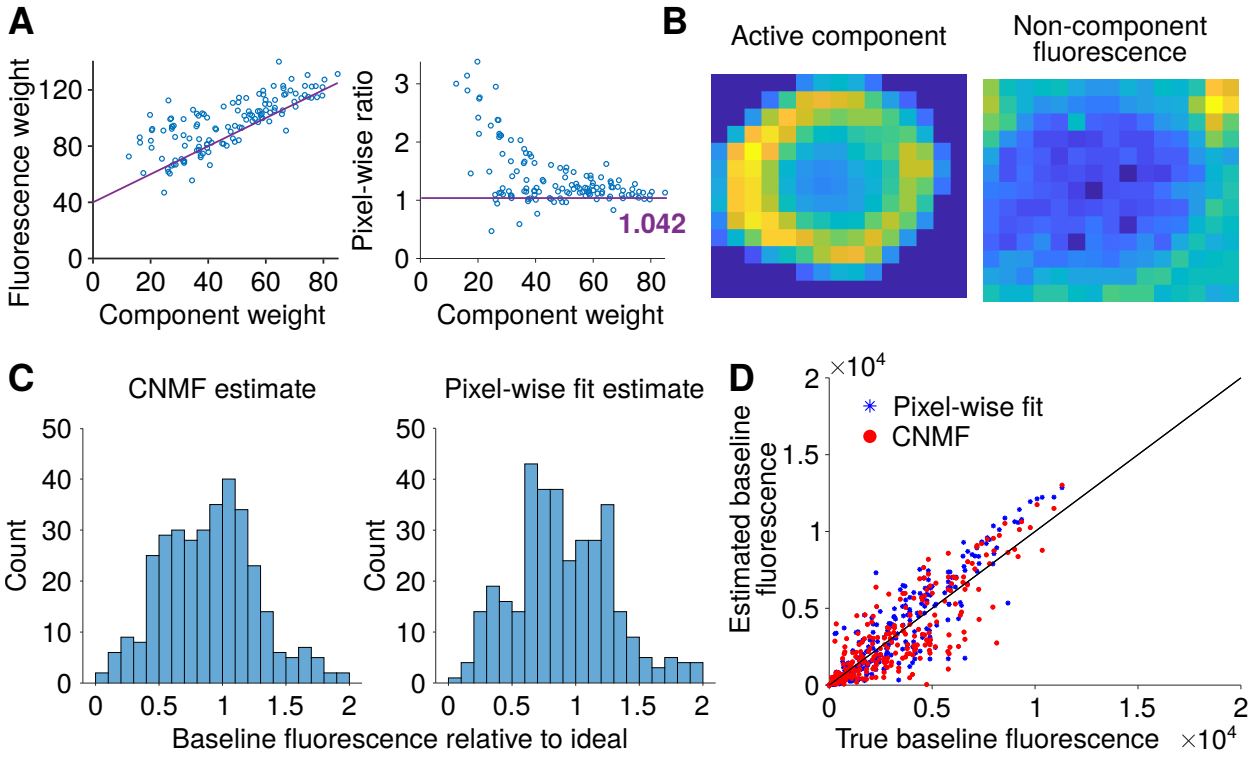

Supplementary Figure 36: Baseline fluorescence ratio estimation validation using NAOMi simulations. A: (Left) Scatterplot of pixel-wise fluorescence of the modal image to the active component fluorescence. Fitted line indicates estimate of minimum noncomponent fluorescence value and slope of component weight. (right) Scatterplot of pixelwise ratio modal values corrected by fitted line to active component fluorescence. B: (Left) Active component fluorescence (Right) estimated corrected noncomponent fluorescence. C: (Left) Histogram of the estimation of the baseline as per CNMF's internal algorithm. (Right) Histogram of the baseline as per a statistical estimate using the internal pixels (see Methods). D: Scatterplot depicting the accuracy of the baseline estimates with respect to the "ground truth" baseline.